Reverse Stark effect, anomalous optical transitions, and control of spin in topological insulator quantum dots

Hongya Xu and Ying-Cheng Lai

Phys. Rev. B **92**, 195120 — Published 11 November 2015

DOI: 10.1103/PhysRevB.92.195120

Reverse Stark effect, anomalous optical transitions, and control of spin in topological insulator quantum dots

Hongya Xu[1] and Ying-Cheng Lai[1,2,*]

[1] *School of Electrical, Computer and Energy Engineering, Arizona State University, Tempe, AZ 85287, USA*

[2] *Department of Physics, Arizona State University, Tempe, Arizona 85287, USA*

(Dated: October 20, 2015)

Formed through a closed domain magnetic heterostructure on the surface of a 3D topological insulator, a quantum dot permits a class of quantized interfacial states of a topological origin. We find that these states exhibit a remarkable, reverse Stark effect in response to an applied electric field. In particular, those topological states whose energies are within the gap exhibit peculiar electrical alignments that are opposite to those associated with the conventional quantum-confined Stark effect, in that the positive (negative) energy states tend to align with (against) the direction of the field. The phenomenon has unusual implications for the associated optical transitions. Furthermore, the exotic topological states exhibit polarized spin textures that can be effectively controlled electrically or optically, opening avenue for potential applications in Dirac material based spintronics.

PACS numbers: 73.21.La, 73.20.At, 71.70.Ej, 71.15.Rf

I. INTRODUCTION

In systems exhibiting the conventional quantum-confined Stark effect (QCSE), e.g., a semiconducting quantum well, an external electrical field shifts the electronic states in the conduction band to lower energies and the hole states in the valence band to higher energies[1]. As a result, the energy differences between the electronic and hole states are narrowed, reducing the frequencies of the permitted photon absorption or emission. In this paper, we report the intriguing phenomenon of reverse Stark effect: in topological Dirac materials an applied electrical field tends to *widen* the energy differences and consequently *increase* the light absorption or emission frequencies.

Uncovering, understanding, and exploiting exotic quantum phases are frontier problems in physics[2]. Recent years have witnessed a great deal of effort in phase phenomena of certain topological origin[3,4]. For example, 2D gapless topological phases were predicted and realized at the interface between bulk Bi_2Se_3 crystal and the vacuum[5], where a change in the Z_2 invariant from the former to the latter occurs. Inducing an energy gap by breaking the time-reversal symmetry in the vicinity of a magnetic material can lead to exotic phases of broken symmetry with dramatic physical consequences[4,6] such as zero-field half-integer quantum Hall effect[3], topological magnetoelectric effect[7], and magnetic monopole[8]. Topological effects in gapped Dirac materials are thus quite intriguing, where topologically protected chiral interfacial states carrying dissipationless currents can arise, which share the same mechanism as that for the Jackiw-Rebbi modes[9]. More recently, it was demonstrated that tuning the topological behaviors through an electric field can lead to quantum spin Hall effect, bringing field-effect topological transistors closer to reality[10].

We investigate the response of the topological states in a confined geometry, e.g., a quantum dot formed on the surface of a 3D topological insulator via a closed magnetic domain heterostructure, to an applied electric field. The system can be described by the Dirac equation subject to proper mass confinement. With an inverted mass profile, a branch of quantized topological edge states can emerge[11]. We find that, when an external electric field is applied, the under-gap topological states exhibit quite unusual alignments: the positive (negative) energy electronic states follow (align against) the direction of the field. As a result, a reverse QCSE occurs in that the frequencies of the permitted light absorption or emission *increase*. Remarkably, these states possess spin textures of ring-like in-plane polarization, which can be effectively controlled electrically or optically. We provide an analysis based on solutions of the Dirac equation to explain these counterintuitive phenomena. The findings can have potential applications in Dirac material based optoelectronics and spintronics.

This paper is organized as follows. In Sec. II, we formulate the theoretical model and demonstrate the emergence of quantized topological edge states. In Sec. III, we investigate the response of the topological edge states to an external electric field, and present the phenomena of reverse electric alignments, electrically controllable spin, and optical transitions. To elaborate on the practical significance of these phenomena, in Sec. IV, we discuss feasible experimental schemes and potential applications.

II. HAMILTONIAN AND QUANTIZED TOPOLOGICAL STATES

Consider a dot geometry formed on the surface of a 3D TI through a nanoscale magnetic heterostructure, as schematically shown in Fig. 1(a). For low energies, the system is described by the following 2D Dirac Hamilto-

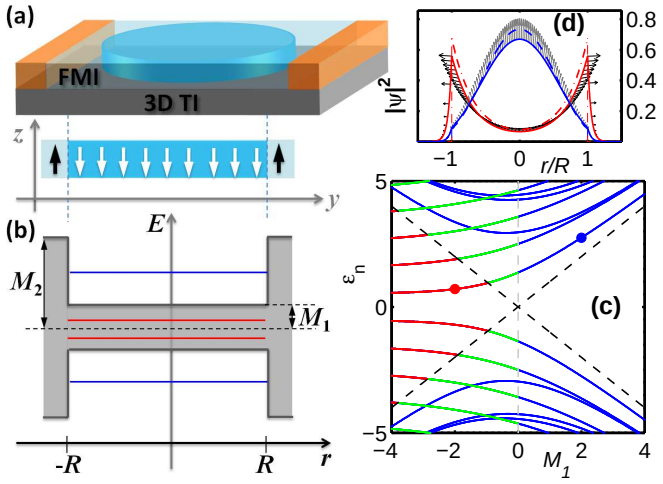

FIG. 1. (Color online). (a) Schematic illustration of a quantum dot formed on the surface of a 3D topological insulator through a closed magnetic domain heterostructure of ferromagnetic insulators (e.g., EuS). (b) Schematic energy diagram of the dot system with mass confinement for zero applied field (R: dot radius; M_1 and M_2: dimensionless masses of the inner and outer regions, respectively). (c) Energy spectra of the dot structure in (b) as a function of M_1 for fixed $M_2 = 10$, where the blue curves denote the normal states and the black dash lines specify the insulating gap boundaries defined by M_1. The emergent edge states through a topological mechanism are divided into the under-gap and over-gap ones, denoted by the red and green curves, respectively. (d) Sectional view of the density distributions of the lowest positive energy states for $M_1 = \mp 2$ as indicated by the red and blue dots in (c). The red and blue curves are for the topological and normal states, respectively. Arrows denote the local spin orientation in the $S_x - S_z$ plane. The dashed/dot-dashed lines correspond to the case of hard-wall confinement, i.e., $M_2 \to +\infty$.

nian[4,12]:

$$\hat{H} = v_F\, \hat{\boldsymbol{\sigma}} \cdot \hat{\boldsymbol{p}} - e\varphi + \mathcal{M}(\boldsymbol{r})\hat{\sigma}_z, \tag{1}$$

where v_F is the Fermi velocity, $\hat{\boldsymbol{\sigma}}$ is the vector of Pauli matrices, $\boldsymbol{p} = (p_x, p_y, 0)$, $\boldsymbol{r} = (x, y, 0)$, the potential φ comes from the applied electric field $\boldsymbol{E} = -\boldsymbol{\nabla}\varphi$, and $-e < 0$ is the charge of an electron. The position dependent "mass" term $\mathcal{M}$ is responsible for the confinement through a time-reversal symmetry breaking mechanism. For simplicity, we assume that the confined region is circularly symmetric with potential jumps at the boundary:

$$\mathcal{M}(r) = \mathcal{M}_1\Theta(R - r) + \mathcal{M}_2\Theta(r - R),$$

where R is the dot radius, as shown in Fig. 1(b), the corresponding energy diagram for the confinement. A constant electric field is applied in the x direction: $\mathcal{E} = \mathcal{E}_0\boldsymbol{e_x}$. In the polar coordinates, the Hamiltonian can be written as $\hat{H} = \hat{H}_0 + \hat{H}_1$, where

$$\hat{H}_0 = \begin{pmatrix} \mathcal{M} & \hat{\mathcal{L}}_- \\ \hat{\mathcal{L}}_+ & -\mathcal{M} \end{pmatrix}, \quad \hat{H}_1 = e\mathcal{E}_0 r\cos\theta, \tag{2}$$

and

$$\hat{\mathcal{L}}_\pm = -i\hbar v_F e^{\pm i\theta}\left(\partial_r \pm i\frac{\partial_\theta}{r}\right).$$

For zero field ($\mathcal{E}_0 = 0$), the z component of the total angular momentum, $\hat{J}_z = -i\hbar\partial_\theta + (\hbar/2)\hat{\sigma}_z$, commutes with $\hat{H}$. As a result, the eigenstates take on the following general form[13]:

$$\langle \boldsymbol{r}|\nu\rangle = \psi_\nu(r,\theta) = \frac{1}{\sqrt{N_\nu}}\exp(il\theta)\begin{pmatrix} f_l(\kappa_\nu r) \\ i\xi_\nu f_{l+1}(\kappa_\nu r)e^{i\theta}\end{pmatrix}, \tag{3}$$

where

$$\xi_\nu = \hbar v_F\kappa_\nu/(\epsilon_\nu + \mathcal{M}),$$
$$\kappa_\nu = \sqrt{\epsilon_\nu^2 - \mathcal{M}^2}/\hbar v_F,$$

and the radial distribution function is $f_l(\kappa_\nu r) = J_l(\kappa_\nu r)$ for $r < R$, and $f_l = \mathcal{C}H_l^{(1)}$ otherwise (J_l and $H_l^{(1)}$ are respectively the Bessel and the Hankel functions of the first kind). Introducing the compact index $\nu = [\tau, ln]$, we can use the integers l and n to specify the orbital angular momentum and the discrete bound states due to the radial confinement, respectively, and $\tau = \pm 1$ to denote the sign of the bound states energies. The eigenvalues $\epsilon_\nu = \varepsilon_\nu\hbar v_F/R$ can be determined by imposing the continuity of the wavefunction $\psi_\nu(r,\theta)$ at $r = R$, and the associated unknown coefficients can be calculated using

$$\mathcal{C} = J_l(\sqrt{\epsilon_\nu^2 - M_1^2}R/\hbar v_F)/H_l^{(1)}(\sqrt{\epsilon_\nu^2 - M_2^2}R/\hbar v_F),$$
$$N_\nu = 2\pi\int_0^\infty r\left[|f_l(\kappa_\nu r)|^2 + |\xi_\nu f_{l+1}(\kappa_\nu r)|^2\right]\mathrm{d}r = R^2A_\nu^2.$$

Figure 1(c) shows, for the zero field case, the dependence of the eigenenergies on the inner region mass (in units of energy) $\mathcal{M}_1 = M_1\hbar v_F/R$ for one fixed value of the outer region mass $\mathcal{M}_2 = 10\hbar v_F/R$. As $\mathcal{M}_1$ changes from positive to negative (in the sense that a sign change in the mass occurs between the inner and outer domains, i.e., $\mathcal{M}_1\mathcal{M}_2 < 0$), a class of new electronic states arise, which are localized at the dot edge. The mechanism behind the formation of these edge states is the Jackiw-Rebbi modes, which are protected by topological changes due to a sign change in the band masses between the two sides of a boundary. The edge states are quantized version of the modes (henceforth the term *quantized Jackiw-Rebbi states*). For the configuration shown in Fig. 1(a), it is thus possible to engineer quantum (electronic) states topologically by tuning the sign of $\mathcal{M}_1$ for a fixed $\mathcal{M}_2$ value, as demonstrated in Fig. 1(c). It is remarkable that the emergent topological states have special spin polarization and carry a dissipationless current. Along with the definition of the spin operator $\hat{\boldsymbol{S}} = \hbar/2(\hat{\sigma}_y, -\hat{\sigma}_x, \hat{\sigma}_z)$, we show in Fig. 1(d) the density distribution and the spin textures of a representative topological state [one marked by the red dot in Fig. 1(c)]. For comparison, we also display a normal state marked by the blue dot

in Fig. 1(c), which is localized within the inner dot domain and exhibits conventional spin polarization due to the given inner region mass. Our goal is to study and understand the response of these quantized topological states to an external electric field.

III. RESULTS

Say the external electric field is along the x direction. Due to lack of a circular symmetry in $\hat{H}$, the eigenstates and eigenenergies can be calculated numerically through an expansion of the state vector: $|\tau, n\rangle = \sum_\nu c_\nu |\nu\rangle$, in terms of the eigenstates $|\nu\rangle$ of the circularly symmetric case ($\mathcal{E}_0 = 0$), where c_ν's are the expanding coefficients. Note that the particle-hole symmetry (i.e., symmetry between the positive and negative energies) is preserved even in the presence of an external electric field[14]. This can be seen by transforming $\hat{H}$ in the Hamiltonian with $\varphi = -\mathcal{E}_0 x$ to $\hat{H}' = U\hat{H}U^\dagger = -\hat{H}$ through the unitary transformation $\hat{U} = \hat{\sigma}_x \mathcal{R}_x$, with $\mathcal{R}_x$ denoting the reflection operation with respect to $x = 0$, provided that the confinement potential $\mathcal{M}(\boldsymbol{r})$ is an even function of x. For the disk geometry considered, the resulting bounded energies occur in symmetric pairs with respect to the zero energy line. For simplicity, we adopt the hard-wall confinement to explicitly generate a set of complete orthogonal basis $\{\epsilon_\nu, |\nu\rangle\}$ and then determine the bound states $\{E_n, |\tau, n\rangle\}$ for a given electric field $\mathcal{E}_0$ through numerical diagonalization of the matrix Hamiltonian $[H_{\mu\nu}]$ of elements

$$H_{\mu\nu} = \delta_{\mu\nu}\epsilon_\nu + \langle\mu|\hat{H}_1|\nu\rangle.$$

For convenience, we use the dimensionless parameter $\lambda = \mathcal{E}_0 R|e|/(\hbar v_F/R)$ to characterize the applied electric field strength and set $\mathcal{M}_2$ to be $+\infty$. The mass potential inside is set as $\mathcal{M}_1 = \pm 2\hbar v_F/R$, which characterizes the normal and topological quantum dot systems, respectively. We use a basis of size about 800 to calculate approximately 50 pairs of bound states with a maximum convergence accuracy of 10^{-6} for any λ within the range of $[-5, 5]$.

A. Reverse electric alignments

The bound-state energies as a function of the dimensionless electric field strength λ are shown in Figs. 2(a) and 2(b) for the normal ($\mathcal{M}_1 = 2\hbar v_F/R$) and the topological ($\mathcal{M}_1 = -2\hbar v_F/R$) cases, respectively. As expected, for both cases, the spectra exhibit the particle-hole symmetry. In addition, there is a Stark shift between levels that have approximate equal energies (quasi-degeneracy), and a stronger field generates a larger shift. A striking phenomenon is that, as λ is increased, the dependence of the under-gap topological bound-state energies on λ (the red curves) exhibits a pattern that is

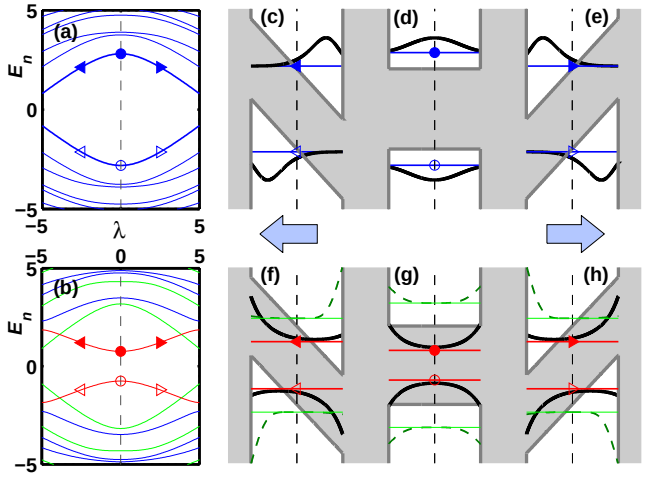

FIG. 2. (Color online) (a,b) Dependence of the bound state energies on the applied electric field strength λ for $M_1 = \pm 2$, respectively. (c-e) Sectional view of the evolution of the normal electronic states [triangles and circles in (a)] for $\lambda = -2.5, 0, 2.5$, respectively. (f-h) Similar to (c-e) but for the topological electronic states indicated in (b) and their adjacent over-gap topological bound states [green (gray) dashed lines]. In (c-h), all the probability density distributions of the indicated electronic states are displaced with solid horizontal lines defining $\langle n, \tau|\tau, n\rangle = 0$ for each curve, while those of the negative energy electronic states are rescaled by -1.

squarely opposite to those for the normal bound states [blue curves, Figs. 2(a) and 2(b)] and for the over-gap topological bound states [green curves, Fig. 2(b)]. We note that the under-gap topological states are in fact the QAHE (quantized anomalous Hall effect) states with the absolute values of energies less than $|\mathcal{M}_1|$ that defines a basic insulating gap for the inner region of the dot. In spite of the fact that these states originate from the same topological mechanism as and share similar edge-localized density distributions with other topological bound states, the effects of an applied electric field can be quite different. This can be further seen from Figs. 2(c-h), where the responses of the corresponding electronic states to the external electric field are shown. For the normal bound states [thick solid lines, Figs. 2(c-e)] and over-gap topological bound states [dashed green lines, Figs. 2(f-h)], we observe the usual alignment behavior: the positive energy electronic states move against the direction of the applied field while the negative energy states move towards the direction of the field. The under-gap topological bound states [thick solid black lines, Figs. 2(f-h)], however, follow the opposite pattern, which is consistent with the behavior observed from the energy spectrum.

To understand the abnormal electric response behavior exhibited by the under-gap topological bound states, we develop a perturbation analysis by treating λ as a small parameter. From the standard time-independent nondegenerate perturbation theory[15], we can calculate

the perturbed energy for a given unperturbed bound state $|\nu\rangle$ up to second order in λ through the expansion $E_\nu = E_\mu^{(0)} + \lambda E_\nu^{(1)} + \lambda^2 E_\nu^{(2)}$. We obtain the corresponding corrections (expressed in dimensionless form):

$$E_\nu^{(0)} = \langle\nu|\hat{H}_0|\nu\rangle = \varepsilon_\nu, \lambda E_\nu^{(1)} = H_1^{\nu\nu},$$

and

$$\lambda E_\nu^{(2)} = \sum_{\mu\neq\nu} \frac{|H_1^{\mu\nu}|^2}{\varepsilon_\nu - \varepsilon_\mu}, \tag{4}$$

where the matrix element $H_1^{\mu\nu}$ is given by

$$H_1^{\mu\nu} \equiv \lambda\langle\mu|\rho\cos\theta|\nu\rangle = \lambda\pi\left[\delta_{l,l'-1} + \delta_{l,l'+1}\right] A_\mu^{-1} A_\nu^{-1} \times \int_0^1 \rho^2 \left[J_{l'}^*(k_\mu\rho) J_l(k_\nu\rho) + \xi_\mu^* \xi_\nu J_{l'+1}^*(k_\mu\rho) J_{l+1}(k_\nu\rho)\right] \mathrm{d}\rho,$$

and $\rho \equiv r/R$, $k_\nu \equiv R\kappa_\nu$. We see that $H_1^{\nu\nu} = 0$ and hence the first order energy correction $E_\nu^{(1)}$ vanishes. To analyze the second order effect and relate it to the numerical results, we focus on the lowest (highest) positive (negative) unperturbed electronic state, i.e., $|1, 01\rangle$ ($|-1, -11\rangle$). From

$$E_\nu^{(2)} = \sum_{\mu\neq\nu} \frac{|\langle\mu|\rho\cos\theta|\nu\rangle|^2}{\varepsilon_\nu - \varepsilon_\mu},$$

we can conclude that the leading term is restricted to two nearest-neighbor states in the energy domain with the angular momentum difference ±1 relative to the given state $|\nu\rangle$, e.g., for $|\nu\rangle = |1, 01\rangle$, $|\mu\rangle \in \{|-1, -11\rangle, |1, \pm11\rangle | \varepsilon_{-1,-11} < 0 < \varepsilon_\nu < \varepsilon_{1,\pm11}\}$. As a result, we can calculate the second order correction to the lowest positive bound-state energy using the approximation

$$E_\nu^{(2)} = \pi\left[\frac{|\mathcal{I}_{\mu_1\nu}|^2}{\varepsilon_\nu - \varepsilon_{\mu_1}} - \frac{|\mathcal{I}_{\mu_2\nu}|^2}{\varepsilon_{\mu_2} - \varepsilon_\nu}\right], \tag{5}$$

where

$$\mathcal{I}_{\mu_1\nu} = \frac{1}{A_{\mu_1} A_\nu} \int_0^1 \rho^2 \mathcal{F}_1(\rho)\mathrm{d}\rho,$$
$$\mathcal{I}_{\mu_2\nu} = \frac{1}{A_{\mu_2} A_\nu} \int_0^1 \rho^2 \mathcal{F}_2(\rho)\mathrm{d}\rho,$$
$$\mathcal{F}_1(x) \equiv J_{-1}^*(k_{\mu_1}x) J_0(k_\nu x) + \xi_{\mu_1}^* \xi_\nu J_0^*(k_{\mu_1}x) J_1(k_\nu x),$$
$$\mathcal{F}_2(x) \equiv J_{\pm1}^*(k_{\mu_2}x) J_0(k_\nu x) + \xi_{\mu_2}^* \xi_\nu J_{\pm1+1}^*(k_{\mu_2}x) J_1(k_\nu x),$$

the sub-indices $\mu_1 = [-1, -11]$, $\nu = [1, 01]$ and $\mu_2 = [1, \pm11]$ denote the relevant states, and the corresponding energies satisfy the relation $\varepsilon_{\mu_1} = -\varepsilon_\nu < 0 < \varepsilon_\nu < \varepsilon_{\mu_2}$. Specifically, for the normal case ($\mathcal{M}_1 = 2\hbar v_F/R$), we have $\mu_2 = [1, 11]$, $M_1 < \varepsilon_\nu = -\varepsilon_{\mu_1} \lesssim \varepsilon_{\mu_2}$ and, hence,

$$(\varepsilon_{\mu_2} - \varepsilon_\nu) \ll (\varepsilon_\nu - \varepsilon_{\mu_1}) = 2\varepsilon_\nu,$$
$$\xi_{\mu_1}^* \xi_\nu = -1$$
$$\xi_{\mu_2}^* \xi_\nu \ll 1.$$

Using these relations, we obtain

$$|\mathcal{I}_{\mu_2\nu}| \sim 2|\mathcal{I}_{\mu_1\nu}|.$$

It is thus straightforward to conclude $E_\nu^{(2)} < 0$ and, consequently, a decreasing energy-field strength relation. For the topological case of $\mathcal{M}_1 = -2\hbar v_F/R$, we see that the states $|\mu_1\rangle$ and $|\nu\rangle$ are the highest negative and the lowest positive under-gap topological states, respectively, while the state $|\mu_2\rangle = |1, -11\rangle$ is an adjacent positive over-gap normal state. Finally, we have

$$(\varepsilon_{\mu_2} - \varepsilon_\nu) > (\varepsilon_\nu - \varepsilon_{\mu_1}),$$
$$|\mathcal{I}_{\mu_2\nu}| \sim |\mathcal{I}_{\mu_1\nu}|/3,$$

leading to $E_\nu^{(2)} > 0$ and hence a reverse dependence of the energies on the strength of the applied field.

B. Optical transition and spin control

The phenomenon of reverse electric field alignments for the under-gap topological bound states and our perturbation analysis suggest the occurrence of abnormal QCSE in our mass confined Dirac system, with potential applications in Dirac material-based optoelectronic and spintronic devices. As a concrete demonstration, we calculate the electric field dependent optical absorption intensity α between the highest negative $|g\rangle$ and the lowest positive $|f\rangle$ energy states, which is determined by dipole matrix element $\boldsymbol{d}_{gf}$ as

$$\alpha \propto |\boldsymbol{v} \cdot \boldsymbol{d}_{gf}|^2, \tag{6}$$

where

$$\boldsymbol{d}_{gf} = \frac{ie\hbar v_F}{E_f - E_g}\langle g|\hat{\boldsymbol{\sigma}}|f\rangle,$$

and $\boldsymbol{v} = (\boldsymbol{e}_x + \boldsymbol{e}_y)/\sqrt{2}$, the polarization vector of the incident light[16,17].

Figure 3 shows the calculated absorption spectra for the normal (blue dots) and topological (red dots) cases, where the sizes of the dots are scaled by the values of the corresponding optical absorption intensity. We see that, in contrast to the normal case where increasing the electric field strength reduces the transition energies and hence the optical absorption frequencies as with conventional QCSE[18], the under-gap topological states generate a small electric field modulated optical absorption rate but, within a certain range of the field strength, lead to an opposite dependence of the transition energy on the field strength.

A remarkable phenomenon is that the spin texture of the topological states [c.f., Fig. 1(d)] renders possible control of spin (and hence the associated magnetic properties) through modulation of the electrical field. To demonstrate this, we calculate the expectation values of the in-plane spin for the topological states,

$$\langle S_{x,y}\rangle = \pm\hbar/2\langle j|\hat{\sigma}_{y,x}|j\rangle$$

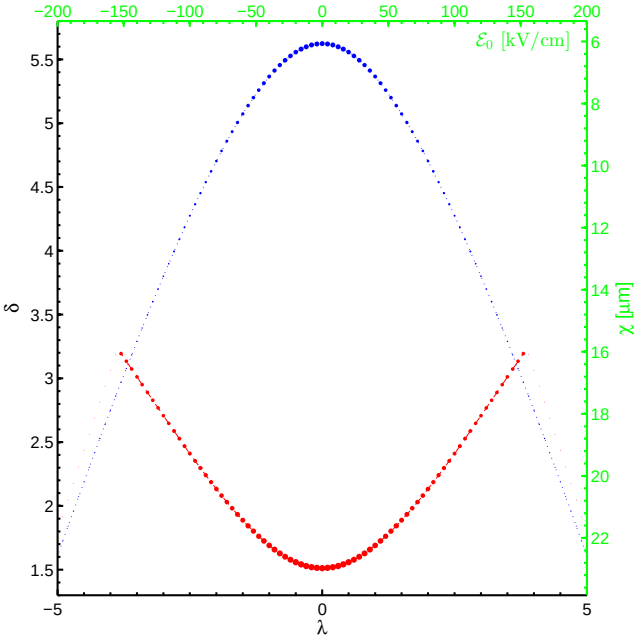

FIG. 3. (Color online) Dipole-induced optical transition rate between states $|g\rangle$ and $|f\rangle$ as a function of the applied electric field strength λ and the transition energy $\Delta E \equiv E_f - E_g = \delta\hbar v_F/R$, where the blue and red dots are for the normal ($\mathcal{M}_1 = 2\hbar v_F/R$) and topological ($\mathcal{M}_1 = -2\hbar v_F/R$) cases, respectively, with the dot size being proportional to the optical absorption intensity α.

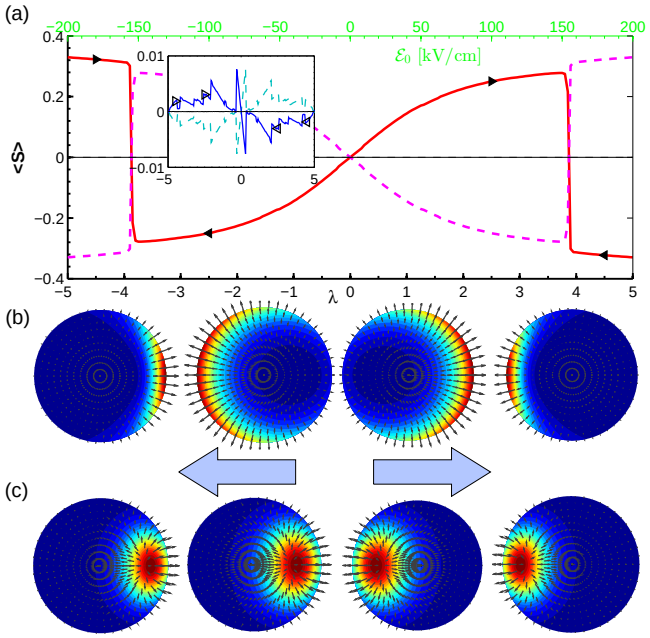

FIG. 4. (Color online) (a) Expectation values of the in-plane spin projection $\langle S_{x,y}\rangle$ of the electronic states $|g\rangle$ and $|f\rangle$ as a function of λ, where the solid-red and dashed-pink lines are $\langle S_x\rangle$ and the gray lines represent $\langle S_y\rangle$. The inset denotes the normal case, where the solid-blue and dashed-cyan lines are for $\langle S_x\rangle$ and the gray lines correspond to $\langle S_y\rangle$. In both cases, the solid lines are for the lowest positive energy electronic state $|f\rangle$, whereas the dashed lines correspond to the highest negative energy electronic state $|g\rangle$. (b,c) Density distributions and spin textures of the state $|f\rangle$ for different values of λ: $-4.5, -2.5, 2.5, 4.5$, from left to right as marked by the solid triangles for the topological case in (b) and by the open triangles for the normal case in the inset of (b), respectively. In both (b) and (c), the color code represents the local probability density, and the gray arrows denote the local in-plane spin orientations.

for $j = g, f$. Figure 4(a) shows the dependence of $\langle S_{x,y}\rangle$ on the electric field strength λ, where the dashed and solid lines are for the states $|g\rangle$ and $|f\rangle$, respectively, and the results for the normal states are included in the inset. Compared with the normal states, the topological states have the intriguing feature that the applied in-plane polarized electric field can modulate the in-plane spins effectively, which is highly desired in spintronics applications. This feature can be further seen in Figs. 4(b) and 4(c), where the evolutions of the spin texture of the state $|f\rangle$ (i.e., the lowest positive energy state) under the applied field in both cases are shown, with the middle and bottom panels corresponding to the topological and normal cases, respectively. The robust optical transition between the under-gap topological states $|g\rangle$ and $|f\rangle$ shown in Fig. 3 indicates that, for a given applied electrical field, it is also possible to control the spin polarizations optically. In fact, Fig. 4(b) shows unequivocally the reverse alignment behavior of the under-gap topological states as analyzed.

IV. EXPERIMENTAL SCHEMES AND POTENTIAL APPLICATIONS

In order to validate and characterize the phenomena uncovered, we articulate a feasible experimental scheme to realize the proposed setup, as shown schematically in Fig. 1(a). From the existing experimental works[6,19–23], we have that the non-uniform mass confinement can be implemented via a closed magnetic heterostructure of ferromagnetic insulators such as EuS, GdN, YIG or $Y_3Fe_5O_{12}$, and $Cr_2Ge_2Te_6$, with different magnetizations of each side deposited on the surface of a 3D topological insulator. Depending on the local exchange coupling of the topological insulator and ferromagnetic insulator as well as the interface quality between them, the magnitude of the induced mass potential can be several to hundred meV[19,21,23]. Interestingly, the sign of the induced mass is tunable by changing the direction of the magnetization

in the ferromagnetic insulator caper layer, which can be achieved by means of the anisotropic feature of the materials[6,22]. The gate electrode can be attached to the topological insulator through which an external electric field can be applied[24].

To discuss the experimental scheme, it is convenient to use the actual physical units of the related dimensionless quantities with specific material parameters. We obtain $\hbar v_F \sim 400\text{meV}\cdot\text{nm}$ for typical TI materials[5], say Bi_2Se_3 or $Pb_xSn_{1-x}Te$. To compare with existing results on the conventional InAs/GaAs self-assembled[18] and HgTe quantum dots[25], we consider a similar dot size, e.g., $R = 10$ nm, where the relevant bound state energies lay within the range of $[-120, 120]$ meV for the mass potential magnitude $|\mathcal{M}_1| \sim 80$ meV. The applied electric field is $\mathcal{E}_0 \sim 40\lambda$ kV/cm, i.e., ranging from -200 kV/cm to 200 kV/cm for $\lambda \in [-5, 5]$. Correspondingly, we obtain the transition energy $\Delta E \sim 40\delta$ meV with the associated wavelength $\sim hc/(40\delta) = 30.996/\delta$ μm. For clarity, we also include these quantities with the related physical units in Figs. 3 and 4(a). We see that the electric field dependent optical transitions for both the conventional and topological cases occur at the mid-infrared (mid-IR) regime in our system, which can be promising for developing reversal QCSE mid-IR optical modulators. Interestingly, for the topological states, the in-plane spin texture can be effectively controlled when varying the applied electric field, thanks to the unusual ring-like spin orientation of the associated topological modes. We remark that the electric field strength analyzed here is actually on the same order of magnitude as that used for the conventional quantum dot systems[18]. Since the bulk band gap of typical materials such as Bi_2Se_3 of about 300 meV[4,5] is indeed much larger than the energy scales of our system, the phenomena uncovered in this paper are potentially experimentally realizable.

V. CONCLUSION

To summarize, we uncover a striking reverse Stark effect in TI based quantum dot systems that permit a class of quantized topological states. With an in-plane electric field, the under-gap topological states exhibit reverse electric alignments, leading to a reverse QCSE phenomenon. We show that the counterintuitive phenomenon can be fully explained by using a second-order perturbation theory. The phenomenon is not only fundamental to relativistic quantum mechanics of Dirac materials, but also practically significant. For example, the reverse Stark effect leads to an inverted optical absorption spectrum, and this anomalous feature can be exploited to develop Dirac material-based optoelectronic devices, e.g., reverse QCSE mid-IR optical modulators. In addition, due to their special spin textures, the in-plane spin degree of freedom of the under-gap topological states can be effectively controlled electrically or optically, opening an avenue for spintronics applications. We further discuss feasible experimental validation schemes and potential applications. Interesting issues to be explored include the effects of symmetry breaking and impurity scattering.

ACKNOWLEDGEMENT

This work was supported by AFOSR under Grant No. FA9550-15-1-0151. and by ONR under Grant No. N00014-15-1-2405.

* Ying-Cheng.Lai@asu.edu

[1] D. Miller, Phys. Rev. Lett. **53**, 2173 (1984).
[2] E. Fradkin, *Field Theories of Condensed Matter Physics*, 2nd ed. (Cambridge University Press, New York, 2013).
[3] X.-L. Qi, T. L. Hughes, and S.-C. Zhang, Phys. Rev. B **78**, 195424 (2008).
[4] M. Z. Hasan and C. L. Kane, Rev. Mod. Phys. **82**, 3045 (2010).
[5] H. Zhang, C.-X. Liu, X.-L. Qi, X. Dai, Z. Fang, and S.-C. Zhang, Nature Phys. **5**, 438 (2009).
[6] P. Wei, F. Katmis, B. A. Assaf, H. Steinberg, P. Jarillo-Herrero, D. Heiman, and J. S. Moodera, Phys. Rev. Lett. **110**, 186807 (2013).
[7] A. M. Essin, J. E. Moore, and D. Vanderbilt, Phys. Rev. Lett. **102**, 146805 (2009).
[8] X.-L. Qi, R. Li, J. Zang, and S.-C. Zhang, Science **323**, 1184 (2009).
[9] R. Jackiw and C. Rebbi, Phys. Rev. D **13**, 3398 (1976).
[10] Q. Liu, X. Zhang, L. B. Abdalla, A. Fazzio, and A. Zunger, Nano Lett. **15**, 1222 (2015).
[11] G. J. Ferreira and D. Loss, Phys. Rev. Lett. **111**, 106802 (2013).
[12] X.-L. Qi and S.-C. Zhang, Rev. Mod. Phys. **83**, 1057 (2011).
[13] A. Gutiérrez-Rubio and T. Stauber, Phys. Rev. B **91**, 165415 (2015).
[14] A. De Martino, D. Klöpfer, D. Matrasulov, and R. Egger, Phys. Rev. Lett. **112**, 186603 (2014).
[15] G. M. M. Wakker, R. P. Tiwari, and M. Blaauboer, Phys. Rev. B **84**, 195427 (2011).
[16] T. Chakraborty and P. Pietiläinen, Phys. Rev. Lett. **95**, 136603 (2005).
[17] D. S. L. Abergel, V. M. Apalkov, and T. Chakraborty, Phys. Rev. B **78**, 193405 (2008).
[18] W. Sheng and J.-P. Leburton, Phys. Rev. Lett. **88**, 167401 (2002).
[19] J. G. Checkelsky, J. Ye, Y. Onose, Y. Iwasa, and Y. Tokura, Nature Phys. **8**, 729 (2012).
[20] A. Kandala, A. Richardella, D. W. Rench, D. M. Zhang, T. C. Flanagan, and N. Samarth, Appl. Phys. Lett. **103**, 202409 (2013).

[21] L. D. Alegria, H. Ji, N. Yao, J. J. Clarke, R. J. Cava, and J. R. Petta, Appl. Phys. Lett. **105**, 053512 (2014).
[22] M. Lang, M. Montazeri, M. C. Onbasli, X. Kou, Y. Fan, P. Upadhyaya, K. Yao, F. Liu, Y. Jiang, W. Jiang, K. L. Wong, G. Yu, J. Tang, T. Nie, L. He, R. N. Schwartz, Y. Wang, C. A. Ross, and K. L. Wang, Nano Lett. **14**, 3459 (2014).
[23] M. Li, C.-Z. Chang, B. J. Kirby, M. E. Jamer, W. Cui, L. Wu, P. Wei, Y. Zhu, D. Heiman, J. Li, and J. S. Moodera, Phys. Rev. Lett. **115**, 087201 (2015).
[24] H. Steinberg, J.-B. Laloë, V. Fatemi, J. S. Moodera, and P. Jarillo-Herrero, Phys. Rev. B **84**, 233101 (2011).
[25] S. Keuleyan, E. Lhuillier, and P. Guyot-Sionnest, J. Ame. Chem. Soc. **133**, 16422 (2011).